

Article

# Influence of Na/Mg Co-Doping in Tuning Microstructure, Transport, Optical, and Magnetic Properties of TiO<sub>2</sub> Compounds for Spintronics Applications

Radha Narzary<sup>1,2</sup>, Bikash Dey<sup>1</sup>, Santanu Sen<sup>1</sup>, Bichitra Nanda Parida<sup>1</sup>, Arunendu Mondal<sup>3</sup>, Seenipandian Ravi<sup>2,\*</sup> and Sandeep Kumar Srivastava<sup>1,\*</sup> <sup>1</sup> Department of Physics, Central Institute of Technology Kokrajhar, Kokrajhar 783370, India<sup>2</sup> Department of Physics, Indian Institute of Technology Guwahati, Guwahati 781039, India<sup>3</sup> Department of Chemistry, Central Institute of Technology Kokrajhar, Kokrajhar 783370, India

\* Correspondence: sravi@iitg.ac.in (S.R.); sk.srivastava@cit.ac.in (S.K.S.)

**Abstract:** In recent years, researchers have been making a persistent effort to discover innovative and appropriate oxide materials that can be exploited in optoelectronics devices. The primary objective of this research is to study the effect of Na/Mg co-doping on microstructure, transport (dielectric and Hall Effect), optical and magnetic properties of Ti<sub>0.94-y</sub>Na<sub>0.06</sub>Mg<sub>y</sub>O<sub>2</sub> (y = 0–0.08) compounds that were synthesized using a solid-state route method. All the compounds have been crystallized to a single rutile phase, as reported by the XRD study. The elemental color mapping reveals that there is a consistent distribution of all of the elements across the compound. The XPS study suggests that Ti mostly resided in the Ti<sup>4+</sup> oxidation state. The enhancement of the Mg co-doping concentration led to a decrease in the dielectric value as well as the AC conductivity of the material. In addition to this, it has been noted that these compounds have a low dielectric loss. The analyses of Nyquist plots reveal that the increase of Mg co-doping concentration led to a rise in the amount of relaxation that is non-Debye sort. This, in turn, caused a reduction in the amount of resistance exhibited by grains and grain boundaries. The Maxwell–Wagner model was used to conduct an analysis of the dielectric data, and the results indicated that the hopping of charge carriers is most likely to be responsible for the transport of electrical charges. From the optical properties' measurement and analyses, it was noticed that the band gap had been slightly changed, but the transmittance value had increased from 81% for Ti<sub>0.94</sub>Na<sub>0.06</sub>O<sub>2</sub> to 84% with an increase in Mg co-doping concentration. The Hall Effect analysis unequivocally pointed to the presence of p-type conductivity as well as an increased carrier density concentration. The room temperature magnetization versus field measurement indicates the ferromagnetic nature of the samples. Thus, the co-doping of Mg with Na in TiO<sub>2</sub> leads to a narrowing of the band gap of TiO<sub>2</sub> while tweaking the optical and transport properties. The studied materials can be utilized for spintronics and optoelectronics applications.

**Keywords:** TiO<sub>2</sub>; d<sup>0</sup> Ferromagnetism; dielectric; optical

**Citation:** Narzary, R.; Dey, B.; Sen, S.; Parida, B.N.; Mondal, A.; Ravi, S.; Srivastava, S.K. Influence of Na/Mg Co-Doping in Tuning Microstructure, Transport, Optical, and Magnetic Properties of TiO<sub>2</sub> Compounds for Spintronics Applications.

*Magnetochemistry* **2022**, *8*, 150.<https://doi.org/10.3390/magnetochemistry8110150>

Academic Editors: Lin Zhu and Kailun Yao

Received: 1 October 2022

Accepted: 2 November 2022

Published: 7 November 2022

**Publisher's Note:** MDPI stays neutral with regard to jurisdictional claims in published maps and institutional affiliations.



**Copyright:** © 2022 by the authors. Licensee MDPI, Basel, Switzerland. This article is an open access article distributed under the terms and conditions of the Creative Commons Attribution (CC BY) license (<https://creativecommons.org/licenses/by/4.0/>).

## 1. Introduction

Researchers have devoted a great deal of time and effort over the past few decades to finding novel materials that can be incorporated into optoelectronic and spintronic systems. Devices like this allow for lower power consumption, faster data processing, non-volatility, and higher storage densities at temperatures higher than room temperature [1,2]. Transition metal (TM)-doped semiconducting oxides have been studied more than any other class of material for their potential use in optoelectronics and spintronic devices. Excellent optical properties and room-temperature ferromagnetism (RTFM) have been discovered in TM-doped semiconducting oxides such as SnO<sub>2</sub>, ZnO, TiO<sub>2</sub>, and ZrO<sub>2</sub> [3–13], which have been studied by a number of laboratories. Moreover, non-magnetic element-doped oxide materials (viz., SnO<sub>2</sub>, TiO<sub>2</sub>, ZnO, LaO<sub>3</sub>) were also found to exhibit excellent optical,

transport, and magnetic properties suggested by a number of ab-initio calculations [14–28] and experimental studies [29–43].

TiO<sub>2</sub>, in particular, has received a lot of focus in the past decade from the field of materials science, alongside other oxides. The three crystalline forms of TiO<sub>2</sub> are called anatase, rutile, and brookite. The crystalline form, rutile, of natural titanium dioxide is very common. Rutile TiO<sub>2</sub> is classified as a tetragonal material with a space group of P4<sub>2</sub>/mnm. Because of its high stability, low cost, lack of toxicity, and exceptional electrical, magnetic, and optical properties, it is being considered for a wide range of uses [41]. The structural, optical, magnetic, and dielectric properties of TiO<sub>2</sub> are sensitive to a wide range of parameters, such as dopant type and purity, growing circumstances, and environmental influences. Doping TiO<sub>2</sub> with a transition metal or a nonmetal can alter its band edge and surface states [12,13]. When the doped element is included in the TiO<sub>2</sub> crystal lattice, new energy levels may be generated between the valence band and the conduction band. Because of the ease with which an outer shell electron can be provided, alkali metals, including calcium, sodium, magnesium, and lithium, are preferred as dopants for TiO<sub>2</sub>. The possibility of d<sup>0</sup> ferromagnetism in TiO<sub>2</sub> by doping with non-magnetic elements has been explored both theoretically and experimentally extensively by researchers. Experimental studies suggest that TiO<sub>2</sub> will exhibit RTFM after being doped with non-magnetic elements like K [24], Mg [26], Cu [28,29], and noble metals like Ag [27]. Recent research has shown that introducing Na dopants into TiO<sub>2</sub> results in a number of exciting new properties, including enhanced conductivity, zero dielectric loss, and room-temperature ferromagnetism [44]. Thus, the obtained results in TiO<sub>2</sub> reveal several intriguing pieces of information which can be useful in spintronics and optoelectronics applications. In this study, we focused on Na/Mg co-doped rutile TiO<sub>2</sub> compounds and analyzed their optical, transport, and magnetic properties. Mg is used as the co-dopant in our investigation because of its identical ionic radii with Ti which helps to stabilize the crystal structure while tweaking the other physical properties. To improve the precision of our characterizations and lessen the frequency of fabrication errors, we synthesized these compounds utilizing a traditional solid-state approach in bulk formation.

## 2. Experimental Details

We used the standard solid-state reaction technique to synthesize Ti<sub>0.94-y</sub>Na<sub>0.06</sub>Mg<sub>y</sub>O<sub>2</sub> (where y = 0, 0.02, 0.04, 0.06, and 0.08) polycrystalline samples. Alfa Aesar's supplied TiO<sub>2</sub> (99.95%), Na<sub>2</sub>CO<sub>3</sub>·H<sub>2</sub>O (99.997%), and MgO (99.95%) were used as raw materials. After the stoichiometric values were determined, the compounds were individually weighed with a digital balance (Model No. BSA323S-CW, Sartorius, Germany). Initially, we used a mortar and pestle to crush and blend the first batch of ingredients, and then we added acetone to verify consistency. After pre-sintering the powdered mixture for 10 h at 300 °C, it was sintered for 20 h at 500 °C and 800 °C. The density of the pelletized samples was increased using a 10-h annealing process at 1000 and 1200 °C. To determine the crystalline phase, a Bruker diffractometer was used to record XRD patterns. Microstructures of the materials were captured by means of a field emission scanning electron microscope (FESEM, Model Sigma, Manufacturer Zeiss). The elemental and color mapping research was carried out with the aid of an energy-dispersive spectrophotometer and a Field Emission Scanning Electron Microscope. Oxidation states of elements in the samples were determined using X-Ray Photoelectron Spectroscopy (Make: Physical Electronics (PHI)& Model: PHI 5000 VersaProbe III), which utilized a highly focused monochromatic X-ray beam of <10 μm to 300 μm. To collect the optical absorption spectra, a Shimadzu UV-VIS spectrophotometer (model number UV-2600) was used. The experiments were carried out between 300 and 800 nm. At room temperature, we measured the dielectric constant, dielectric loss, impedance, and AC conductivity. In each test, frequencies between 100 Hz and 5 MHz were applied. The pellet was given a coating of silver paste that would conduct electricity and then placed in a sample container that was connected to an impedance tester. Finally, the pellet was placed in the sample container of the dielectric measurement system (Model: PSM-1735;

4NL-LC, Loughborough, UK). To count and quantify charge carriers, hall effect measurements were performed in a Van der Pauw setup at room temperature. A commercial SQUID Quantum Design magnetometer (Model: VersaLab, MPMS XL, San Diego, CA, USA) was utilized to capture the M-H hysteresis loop responses.

### 3. Results and Discussions

The formation of the crystalline phase of these prepared materials was identified through the structural study by recording XRD patterns. The detailed crystal structure study is reported elsewhere [44]. The analyses of the XRD patterns indicate that the materials have been formed in a tetragonal rutile-type crystal structure of  $\text{TiO}_2$ . The typical cell parameters of  $\text{Ti}_{0.94}\text{Na}_{0.06}\text{O}_2$  are estimated to be  $a = b = 4.5917 \text{ \AA}$  and  $c = 2.9585 \text{ \AA}$ . The mean crystallite sizes ( $S_c$ ) of all the synthesized polycrystalline compounds were estimated to be in the range of 60–80 nm.

#### 3.1. Microstructure Study by SEM and Compositional Study by EDS

High-resolution FE-SEM was used to conduct the microstructural investigation of the samples. The typical SEM micrographs of  $\text{Ti}_{0.90}\text{Na}_{0.06}\text{Mg}_{0.04}\text{O}_2$  and  $\text{Ti}_{0.86}\text{Na}_{0.06}\text{Mg}_{0.08}\text{O}_2$  are illustrated in Figure 1a,b, respectively. As observed from the SEM micrographs, the morphology of all Na/Mg co-doped compounds is homogenous. The particles in the compound have an approximately circular form, and they are nanoscale in size. Through the use of the Image J program and a Gaussian fitting of the particle size distribution acquired from several SEM micrographs, the particle size was determined and subsequently estimated. The average particle size was somewhere in the region of 20 to 70  $\mu\text{m}$  for these compounds. The Gaussian fitting for  $\text{Ti}_{0.86}\text{Na}_{0.06}\text{Mg}_{0.08}\text{O}_2$  is demonstrated in Figure 1c, and the particle size is determined to be 47  $\mu\text{m}$  according to the graph. It was feasible to deduce the elemental composition and distribution of materials observed in scanning electron microscopy by employing color mapping derived from the EDS spectrum. Figure ??a depicts an example of a combined elemental color mapping for the  $\text{Ti}_{0.90}\text{Na}_{0.06}\text{Mg}_{0.04}\text{O}_2$  compound, whereas Figure ??b–e shows the color mappings for each of the four individual constituent elements individually. Compounds containing all elements are shown to be evenly distributed by the color mapping of the elemental distribution. Table 1 shows the atomic percentage of elements experimentally observed from EDS for  $\text{Ti}_{0.94-y}\text{Na}_{0.06}\text{Mg}_y\text{O}_2$  for  $y = 0, 0.02, 0.04, 0.06,$  and  $0.08$  compounds. Moreover, the final synthesized compounds have no unwanted detectable magnetic impurities like Co or Fe, as shown by EDS analysis. The elemental composition is also very similar to the nominal concentration of the sample under study.

**Table 1.** Estimated cationic ratio of elements present in  $\text{Ti}_{0.94-y}\text{Na}_{0.06}\text{Mg}_y\text{O}_2$  ( $y = 0, 0.02, 0.04, 0.06,$  and  $0.08$ ) compounds as measured by energy dispersive spectroscopy (EDS).

Prepared Sample	Calculated Cationic Ratio (%)		
	Ti	Na	Mg
$\text{Ti}_{0.94}\text{Na}_{0.06}\text{O}_2$	93.8	6.2	0
$\text{Ti}_{0.92}\text{Na}_{0.06}\text{Mg}_{0.02}\text{O}_2$	91.7	6.1	2.2
$\text{Ti}_{0.90}\text{Na}_{0.06}\text{Mg}_{0.04}\text{O}_2$	90.2	5.9	3.9
$\text{Ti}_{0.88}\text{Na}_{0.06}\text{Mg}_{0.06}\text{O}_2$	87.7	6.1	6.2
$\text{Ti}_{0.86}\text{Na}_{0.06}\text{Mg}_{0.08}\text{O}_2$	85.8	6.1	8.1

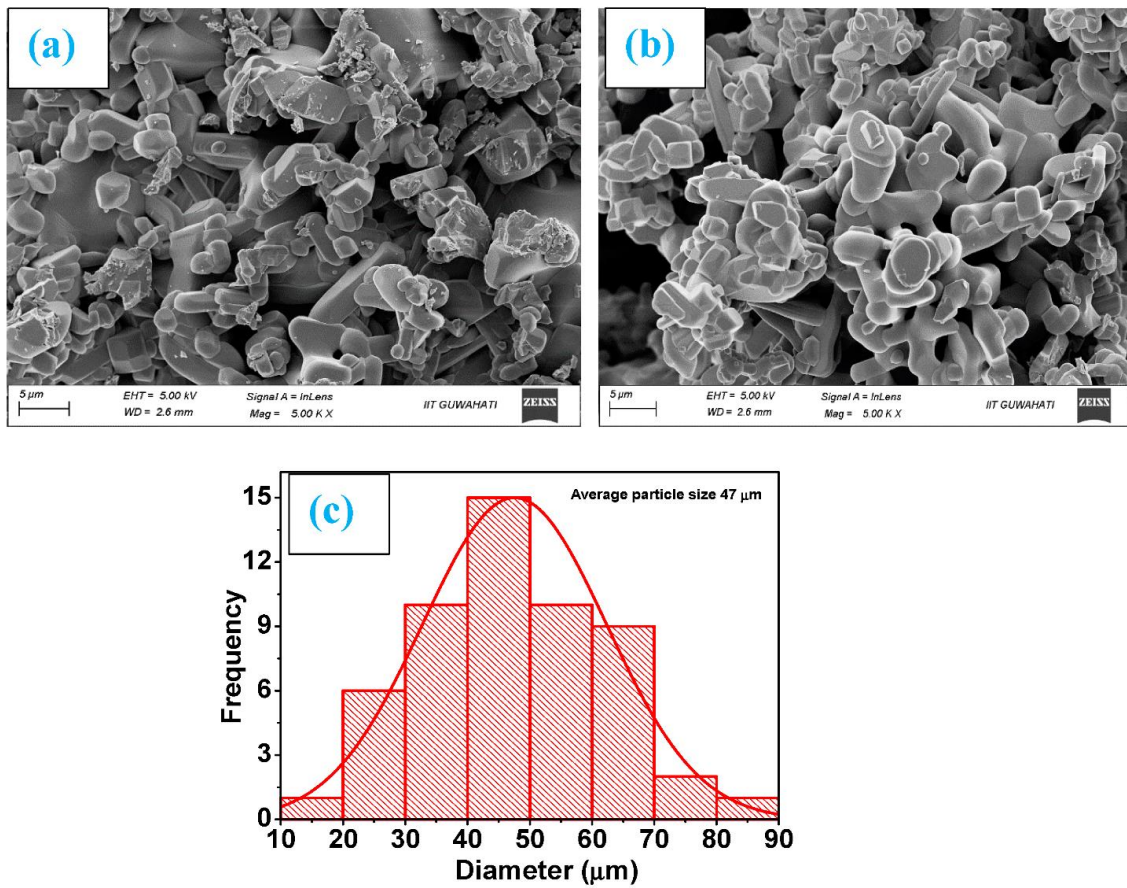


Figure 1. Morphology images as measured by SEM for (a)  $\text{Ti}_{0.90}\text{Na}_{0.06}\text{Mg}_{0.04}\text{O}_2$  and (b)  $\text{Ti}_{0.86}\text{Na}_{0.06}\text{Mg}_{0.08}\text{O}_2$  compounds and (c) the fitting of a Gaussian function to the particle size distribution of  $\text{Ti}_{0.86}\text{Na}_{0.06}\text{Mg}_{0.08}\text{O}_2$  compound.

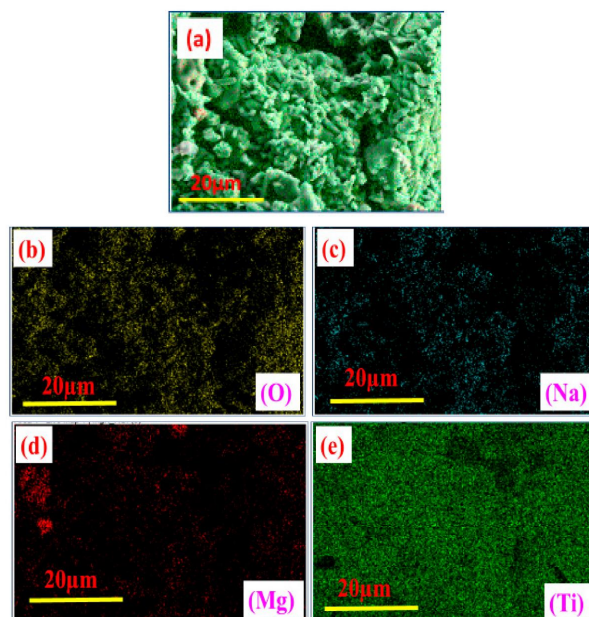
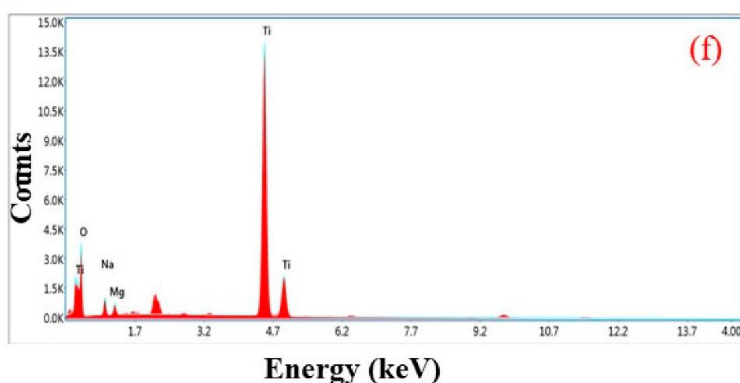


Figure 2. Cont.



**Figure 2.** (a) Elemental color mapping of  $\text{Ti}_{0.90}\text{Na}_{0.06}\text{Mg}_{0.04}\text{O}_2$  compound; (b–e) correspondingly exhibit the individual color mappings for the elements O, Na, Mg, and Ti; and (f) EDAX spectrum of  $\text{Ti}_{0.90}\text{Na}_{0.06}\text{Mg}_{0.04}\text{O}_2$  compound.

### 3.2. X-ray Photoelectron Spectroscopy (XPS)

The X-ray photoelectron spectroscopy (XPS) method is a sensitive surface analysis technique that may be used to effectively probe the surface composition and chemical states of solid samples. The oxidation state and surface chemical composition of Na/Mg co-doped  $\text{TiO}_2$  compounds were measured by XPS. Images of the X-ray photoelectron spectroscopy (XPS) of a sample of  $\text{Ti}_{0.88}\text{Na}_{0.06}\text{Mg}_{0.06}\text{O}_2$  are displayed in Figure 3. Most of the C1s peak at 284.6 eV is a direct result of atmospheric pollution. Titanium, oxygen, magnesium, and sodium can all be seen in the XPS spectrum shown in Figure 3a, suggesting that they are all present at the surface. The binding energies of  $\text{Ti } 2_{p3/2}$  and  $\text{Ti } 2_{p1/2}$  were measured to be at 457.88 and 463.69 eV, respectively, as shown in Figure 3b, suggesting that Ti mostly resided in the  $\text{Ti}^{4+}$  oxidation state [25]. Figure 3d displays XPS spectra of the O 1s area. Three peaks, with binding energies of about 529.32 eV, 530.23 eV, and 531.47 eV, can be used to fit the O 1s spectra, which corresponds to lattice oxygen in  $\text{TiO}_2$  oxygen in  $\text{Ti}_2\text{O}_3$  (O- $\text{Ti}^{3+}/\text{Ti}^{4+}$ ) and hydroxyl group (-OH) oxygen, respectively. It is shown in Figure 3c the XPS spectra of the Mg 2s area. Two binding energy peaks, at 87.58 eV and 101.62 eV, are visible in the spectra of the Mg 2s. These two Gaussian peaks, at 87.58 and 101.62 eV, respectively, reflect  $\text{Mg}^{2+}$  ions occupying octahedral and tetrahedral positions in the Mg 2s peak. Na 1s XPS spectra are displayed in Figure 3e. Specifically, Na 1s has a binding energy maximum of 1071.07 eV.

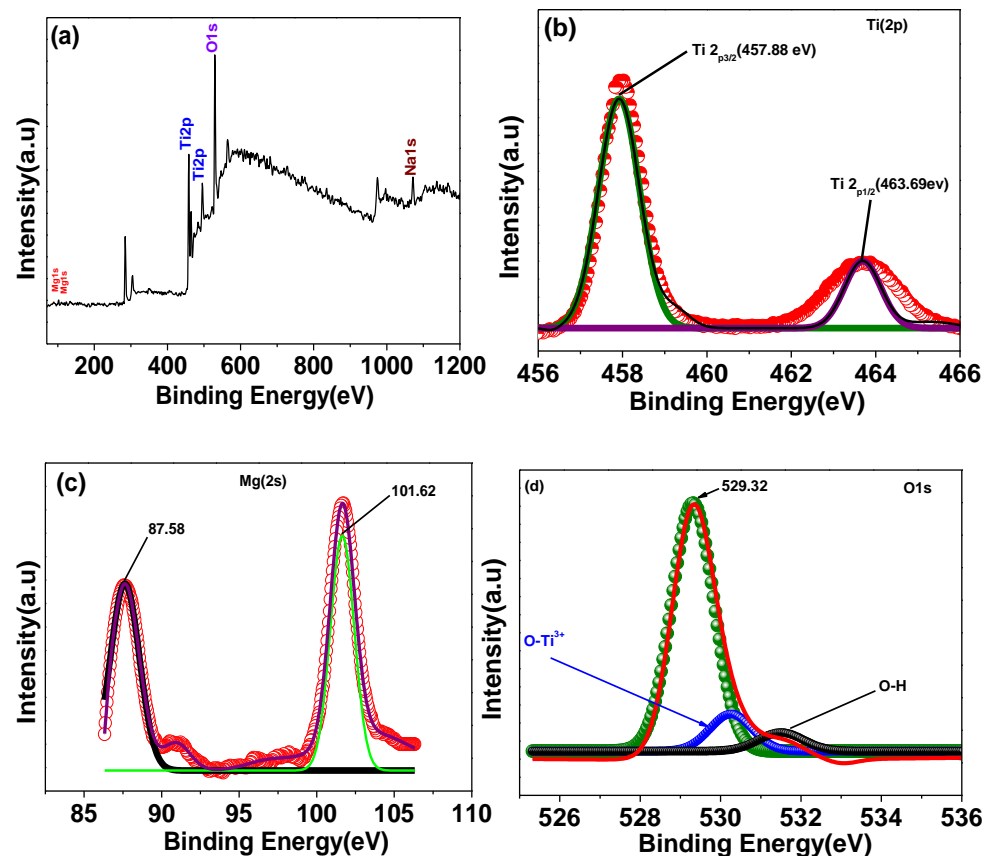


**Figure 3.** XPS spectra of (a)  $\text{Ti}_{0.88}\text{Na}_{0.06}\text{Mg}_{0.06}\text{O}_2$  compound, (b) Ti 2p peak, (c) Mg 2s peak, (d) O 1s peak, and (e) Na 1s peak of  $\text{Ti}_{0.88}\text{Na}_{0.06}\text{Mg}_{0.06}\text{O}_2$  compound, respectively.

### 3.3. Dielectric Constant ( $\epsilon_r$ ), Loss Tangent ( $\tan\delta$ ), Complex Impedance, and AC Conductivity

#### 3.3.1. Dielectric Constant ( $\epsilon_r$ )

Figure 4 depicts the frequency-dependent dielectric constant ( $\epsilon_r$ ) for all Na/Mg co-doped  $\text{TiO}_2$  compounds. The initial  $\epsilon_r$  value of all substances has been observed to decrease with increasing frequency. At higher frequencies, however, a flat response curve is observed, which suggests that the  $\epsilon_r$  value does not change drastically. Because of this, it is possible that each of the new compounds will show some degree of dielectric dispersion. Dielectric constant readings are large at low frequencies and decrease with increasing frequency, indicating a dielectric transition in the sample. Further, the dielectric constant is largest at low frequencies and decreases with increasing frequency. The interfacial polarisation, dipolar polarisation, ionic polarisation, and electronic polarisation that make up the total polarisation are what we need to discuss in order to understand what's behind the observed dielectric behavior shift in the sample [45]. When an external AC electric field is applied, and all-electric dipoles are aligned in that direction of the field, the dielectric constant is at its maximum value at low frequencies. However, the contribution of ionic and dipolar polarisation to the total polarisation computation decreases as the frequency increases because relatively heavy particles become unable to follow the applied electric field. However, at higher frequencies, the contribution of grain boundaries becomes more noticeable as a result of the accumulation of defects such as impurities and deficiencies as well as thermally activated charge carriers, which together increase the value of interfacial polarisation first introduced by Maxwell–Wagner [45]. Their proposed model included a grain boundary layer and a layer of well-conducting grains. At high frequencies, electron activity increases at grain boundaries, while at low frequencies, it decreases. This indicates that the grain boundaries are a very resistant region. Dielectric loss is minimized as a result since the dielectric constant has the smallest value at higher frequencies.

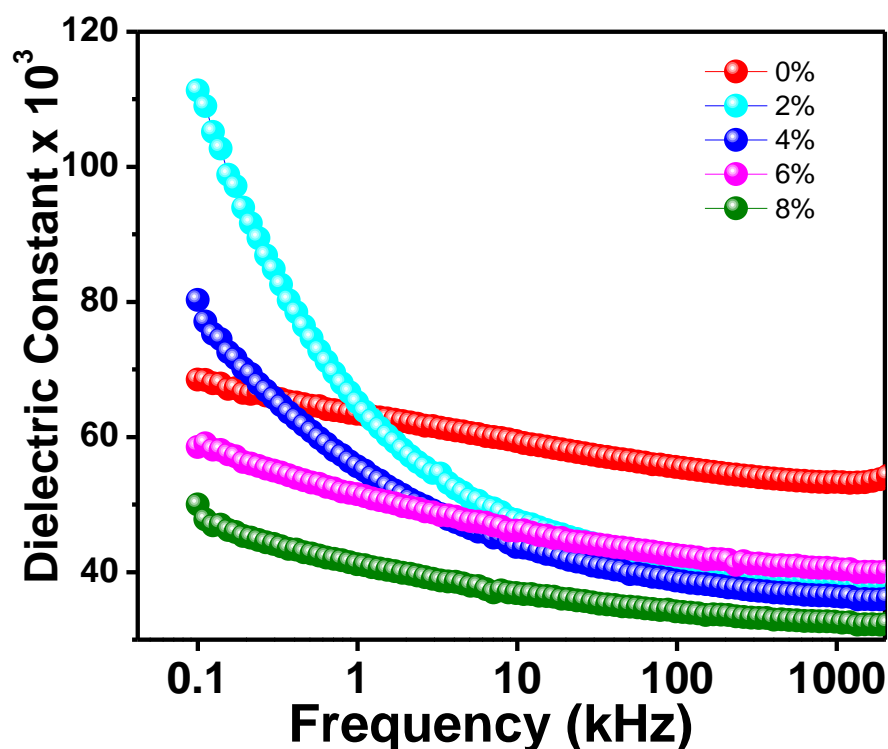


**Figure 4.** The frequency variation of dielectric constant of  $\text{Ti}_{0.94-y}\text{Na}_{0.06}\text{Mg}_y\text{O}_2$  with  $y = 0, 0.02, 0.04, 0.06,$  and  $0.08$  compounds.

### 3.3.2. Dielectric Loss

Figure 5 depicts the variation of loss tangent ( $\tan\delta$ ) with applied AC frequency for all Na/Mg co-doped  $\text{TiO}_2$  compounds. As can be observed from the graph, the value of the dielectric loss drops by a significant amount as the alternating current frequency is increased. On the other hand, the value of  $\tan\delta$  remains essentially constant as it gets closer and closer to zero as the frequency increases. The Maxwell–Wagner model combined with Koop’s theory can provide a satisfactory explanation for this fluctuation in the loss tangent value with increasing frequency [45]. At lower frequencies, the concentration of charge carriers keeps on rising as a result of the extraordinarily active nature of the insulating grain boundaries. As a consequence of this fact, a greater amount of energy is required to transport the charge carriers through the grain boundaries, which eventually results in a greater degree of dielectric loss. Charge carriers are able to flow easily at the grains because semiconducting grains are more active at higher frequencies. Despite the fact that the frequency is greater, there is not a significant loss of energy as a result of this free flow of charge carriers. This leads to a smaller dielectric loss. In addition, within the specified frequency range, none of the curves that we generated for our studies exhibited any kind of loss peak. One possible explanation for the absence of a peak is that the dielectric permittivity makes only a small contribution to any frequency-dependent changes in the dielectric loss. Because there was no dielectric loss in the samples that were prepared, it is clear that these materials have the potential to be utilized in high-frequency optoelectronic devices.

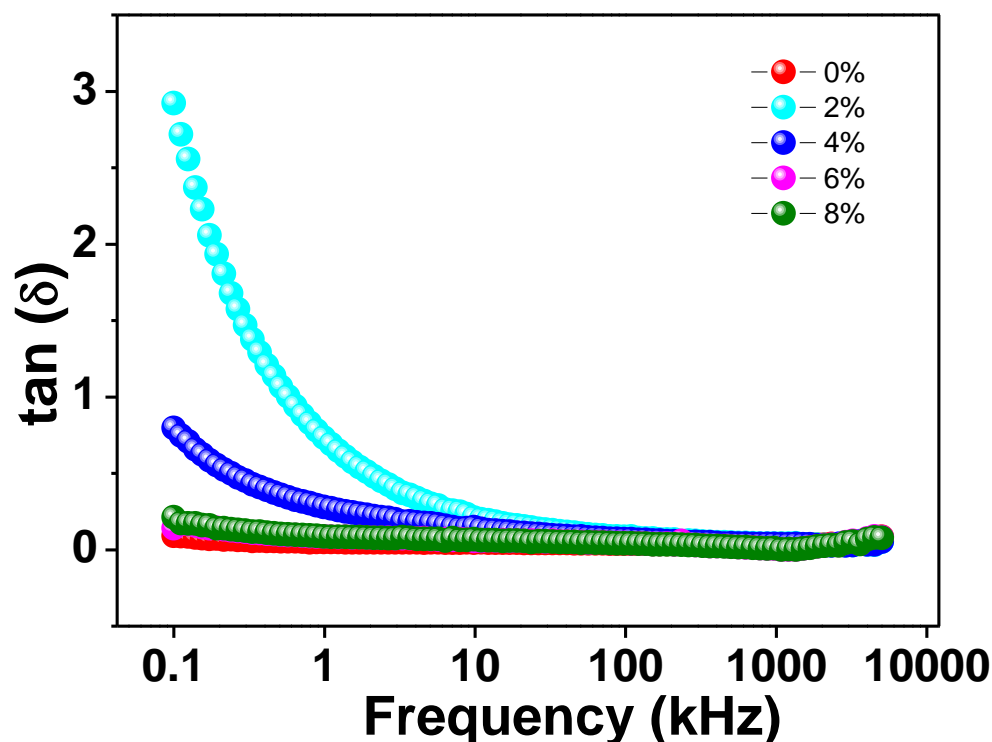


**Figure 5.** The frequency variation of tangent loss of  $\text{Ti}_{0.94-y}\text{Na}_{0.06}\text{Mg}_y\text{O}_2$  with  $y = 0, 0.02, 0.04, 0.06,$  and  $0.08$  compounds.

### 3.3.3. Complex Impedance Analysis (CIA)

The frequency dependence of the real and imaginary parts of the alternating current impedance ( $Z'$  and  $Z''$ ) is depicted in Figure 6a,b, respectively for  $\text{Ti}_{0.94-y}\text{Na}_{0.06}\text{Mg}_y\text{O}_2$  where  $y = 0, 0.02, 0.04, 0.06,$  and  $0.08$ . The plots show that as frequency increases,  $Z'$  decreases consistently up to a limiting range of roughly 10 kHz and then almost stops depending on the frequency at higher frequencies. The material is shown to have both linear and circular polarisation in this way. However, at lower frequencies, a larger value of  $Z'$  is seen, suggesting that the materials are highly polarised.  $Z''$ , the imaginary part of the impedance, exhibits a similar pattern of variation, contingent upon the frequency being employed. The graph clearly shows that as Na/Mg co-doping levels in  $\text{TiO}_2$  rise, the imaginary component of the overall impedance falls, and the peak frequency moves down the spectrum. The conductivity increases as the imaginary part of the impedance decreases, and the peak shifts, indicating that Mg co-doping grows as the material relaxes. The decrease in the imaginary part of the impedance with increasing Mg co-doping reflects the increased accessibility of the charge carriers to the alternating current electric field.

Complex impedance analysis (CIA), which makes use of Nyquist plots, can be helpful for understanding the effects of grains, grain boundaries, and likely electrode effects on the capacitive, reactive, resistive, and inductive properties of the materials. This research allows us to disentangle the roles played by grains and grain borders in the overall impedance of the material. The Nyquist pattern for compounds with  $y = 0, 0.02, 0.04, 0.06,$  and  $0.08$  of  $\text{Ti}_{0.94-y}\text{Na}_{0.06}\text{Mg}_y\text{O}_2$  at room temperature is shown in Figure 7. It shows that the resistance of  $\text{Ti}_{0.94-y}\text{Na}_{0.06}\text{Mg}_y\text{O}_2$  compounds has grown gradually as the Mg concentration is reduced, as evidenced by a narrower semicircle in the Nyquist plot. This resistance value has a substantial effect on the real and imaginary parts of the impedance's amplitude. When fitting the Nyquist plot, it is necessary to select a suitable comparable circuit model. The electrical properties of the material are described by a series-connected two-leg equivalent circuit. These branches are meant to depict the electrical properties of the material at the grain boundaries as well as within the grains themselves. By employing the ZSimpWin

application, one may display the properties of each component of the comparable circuit depicted in Figure 8.

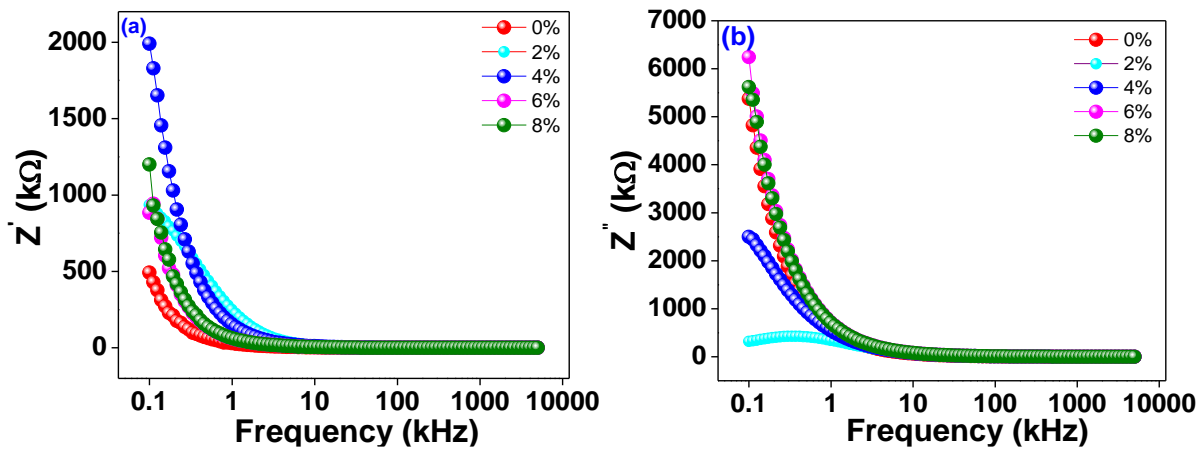


**Figure 6.** (a) The frequency variation of real part of ac impedance  $Z'$ . (b) The frequency variation of imaginary part of AC impedance  $Z''$  of  $\text{Ti}_{0.94-y}\text{Na}_{0.06}\text{Mg}_y\text{O}_2$  with  $y = 0, 0.02, 0.04, 0.06, 0.08$  compounds.

To separate the effects of grains from those of grain boundaries, we employed a series combination of two parallel circuits.  $R_g$  and  $C_g$ , which stand for the grain resistance and capacitance, respectively, are connected in series in the first parallel circuit. In the second parallel circuit,  $R_{gb}$ ,  $C_{gb}$ , and CPE stand for the grain boundary resistance, grain boundary capacitance, and constant phase element, respectively. The factors taken into account while modeling analogous circuits are tabulated in Table 2. Evidence suggests that  $R_g$  and  $R_{gb}$  both decline with increasing co-doping concentration, which points to a general decrease in  $R$  across the boundary in the samples. It can be inferred from the decreasing  $R_g$  and  $R_{gb}$  numbers. The high  $R$  effects on carrier flow between the metal and the semiconductor could be a contributing factor. The interface between metal and semiconductor may be rough or have a lattice mismatch, which would have the same effect [46,47].

**Table 2.** Equivalent circuit parameters of the complex impedance plots of  $\text{Ti}_{0.94-y}\text{Na}_{0.06}\text{Mg}_y\text{O}_2$  for  $y = 0, 0.02, 0.04, 0.06, \text{ and } 0.08$ .

Mg Concentration (%)	$R_g$ ( $\Omega$ )	$R_{gb}$ ( $10^8 \Omega$ )	$C_g$ ( $10^{-9}$ F)	$C_{gb}$ ( $10^{-10}$ F)
0	1011	3.96	5.20	2.38
2	54	0.01	4.58	1.76
4	3531	0.09	2.73	1.67
6	8000	2.73	9.12	0.01
8	10,000	1.73	1.05	1.69

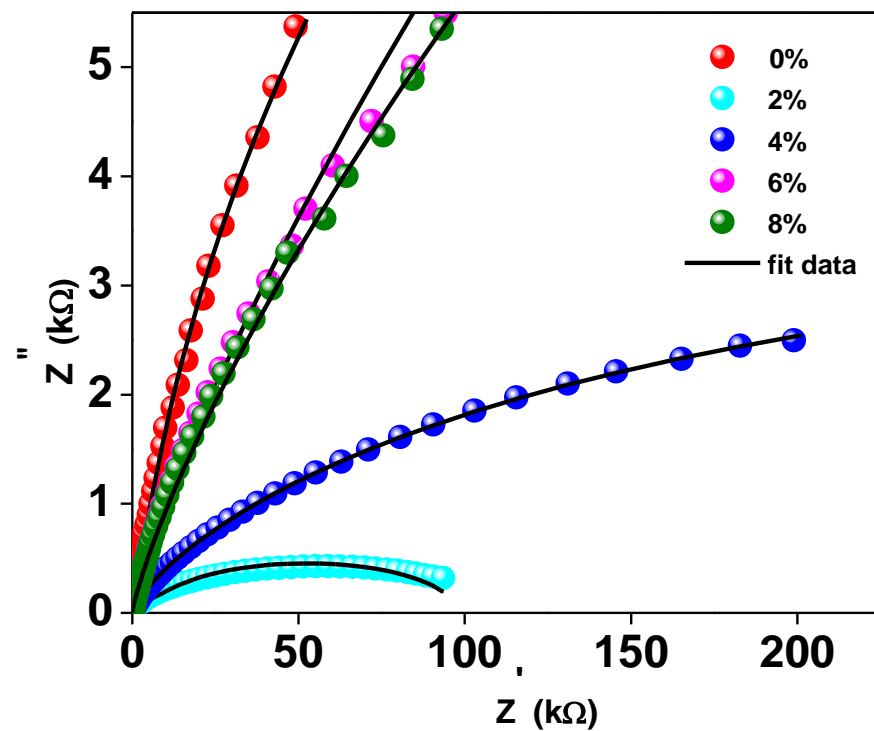


Figure 7. The Nyquist Plot of  $\text{Ti}_{0.94-y}\text{Na}_{0.06}\text{Mg}_y\text{O}_2$  with  $y = 0, 0.02, 0.04, 0.06, 0.08$  compounds.

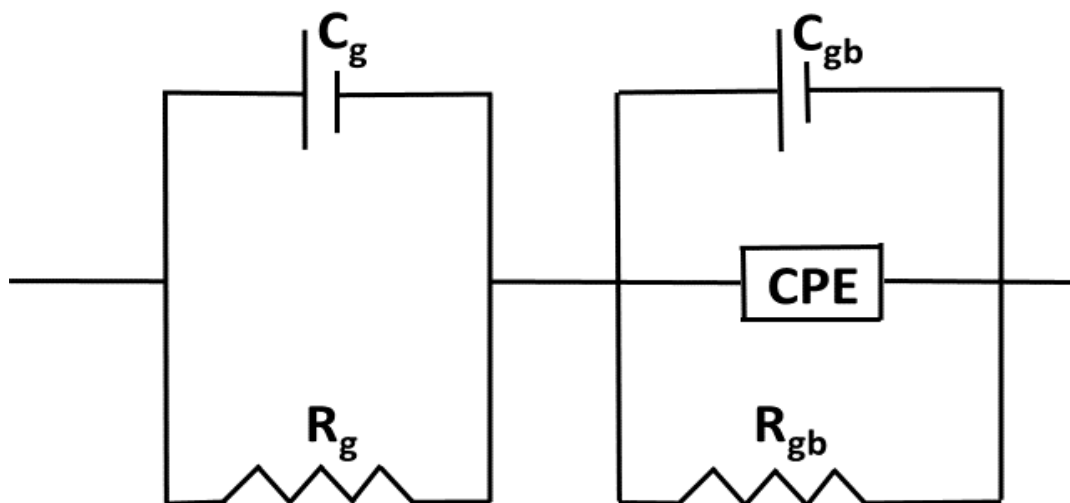


Figure 8. The Equivalent circuit model for Nyquist Plot of  $\text{Ti}_{0.94-y}\text{Na}_{0.06}\text{Mg}_y\text{O}_2$  with  $y = 0, 0.02, 0.04, 0.06, 0.08$  compounds.

### 3.3.4. AC Conductivity

Figure 9 graphically depicts the correlation between the applied frequency and the AC conductivity of every Na/Mg co-doped  $\text{TiO}_2$  compound. The AC conductivity is nearly constant as a function of frequency up to  $10^2$  Hz, but then the figure shows a distinct increase in conductivity. This data indicates that increasing the Mg co-doping concentration in the  $\text{TiO}_2$  compound will enhance the material's AC conductivity at higher frequencies. It has been suggested that the hopping model [45] can provide an explanation for the observed pattern of behavior in AC conductivity. At low frequencies, transport occurs along a virtually infinite channel, resulting in an extremely low value for AC conductivity. As a consequence, the rate at which they hop is reduced. It has been found that increasing the frequency of the alternating current flowing through a material increases the pace at

which charge carriers hop. This results in an increase in the AC conductivity of the material due to an increase in the hopping of charge carriers.

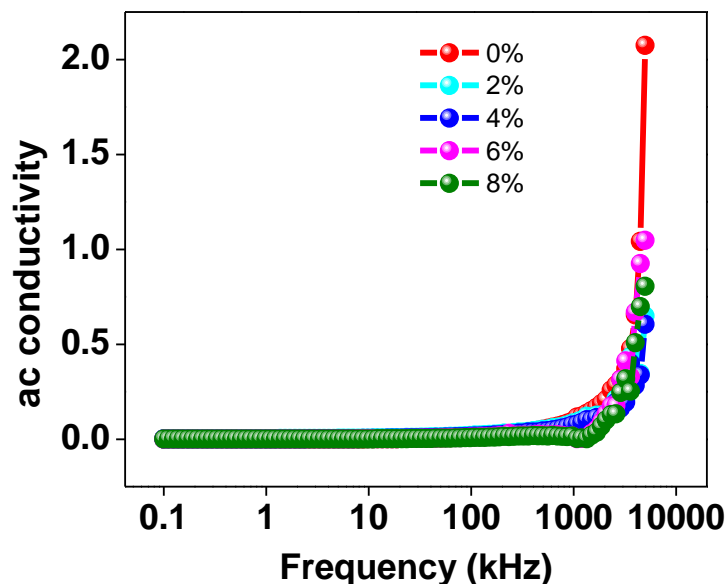


Figure 9. The frequency variation of AC conductivity of  $Ti_{0.94-y}Na_{0.06}Mg_yO_2$  with  $y = 0, 0.02, 0.04, 0.06, 0.08$  compounds.

### 3.4. Hall Effect Measurement

For the purpose of determining the carrier density and the kind of doping present in  $Ti_{0.94-y}Na_{0.06}Mg_yO_2$  with  $y = 0, 0.02, 0.04, 0.06, 0.08$  compounds, a Van der Pauw configuration was utilized for the Hall effect measurement. According to the findings of this investigation, the conductivity of all Na/Mg co-doped  $TiO_2$  compounds is p-type. Hole density (also called carrier density) increases with Mg concentration, as shown in Figure 10. The production of holes results from the substitution of Mg atoms for Ti atoms because Mg has a lower valency state than Ti ions. As a whole, the carrier density for all Na/Mg co-doped  $TiO_2$  compounds is estimated to range between  $1-4 \times 10^{13} / cm^3$ .

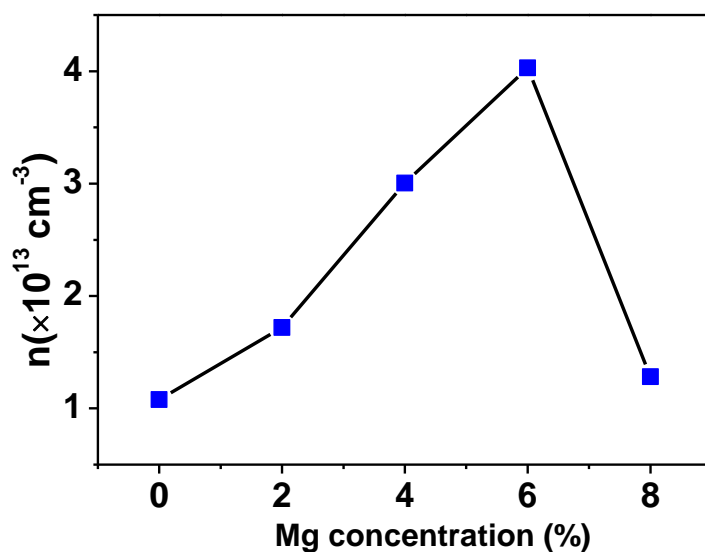


Figure 10. Variation of carrier density in  $TiO_2$  with Na/Mg co-doping concentrations.

### 3.5. Optical Properties

The optical absorbance spectra of  $\text{Ti}_{0.94-y}\text{Na}_{0.06}\text{Mg}_y\text{O}_2$  compounds with  $y = 0, 0.02, 0.04, 0.06, 0.08$  were obtained by using a UV Visible spectrophotometer to collect data in the 300–700 nm wavelength region. The UV absorption edge in the  $\text{Ti}_{0.94}\text{Na}_{0.06}\text{O}_2$  compound's absorption spectra can be seen at 350 nm, as illustrated in Figure 11a. This could be owing to  $\text{TiO}_2$ 's inherent band gap absorption, which occurs as a result of electronic transitions from the valence band to the conduction band ( $\text{O}_{2p}$  to  $\text{Ti}_{3d}$ ). The energy band gap of the materials is calculated using Tauc and Davis  $(\alpha h\nu)^2 = (h\nu - E_g)$  Mott method for direct band gap semiconductors [48]. This formula was created for direct band gap semiconductors. In this equation,  $\alpha$  represents the absorption coefficient,  $h$  the Planck constant,  $\nu$  the photon frequency, and  $E_g$  the semiconductor's optical band gap. Figure 10 illustrates a Tauc's plot, which was constructed by graphing  $(\alpha h\nu)^2$  as a function of photon energy  $h\nu$ , which was collected from all of the samples' absorption spectra. The values of band gap  $E_g$  are discovered at the place where the straight line on the x-axis of the Tauc plots makes an intercept. The band gap energy in  $\text{Ti}_{0.94}\text{Na}_{0.06}\text{O}_2$  is 2.67 eV, which is similar to the typical value discovered in a recent work [44]. The energy band gap for  $\text{TiO}_2$  compounds with 2%, 4%, 6%, and 8% Na/Mg co-doping is 2.70 eV, 2.73 eV, 2.50 eV, and 2.45 eV, as illustrated in Figure 12a–e, respectively. The fluctuation of the band gap in  $\text{TiO}_2$  with Na/Mg co-doping concentrations is shown in Figure 10f. As a result, calculating the band gap of Na/Mg co-doped  $\text{TiO}_2$  compounds shows that the band gap in  $\text{TiO}_2$  compounds decreases as the amount of Na/Mg co-doping increases. This extra decrease in the energy band gap of the  $\text{TiO}_2$  compound in the presence of Mg co-doping could be attributed to the formation of a thin impurity band inside the forbidden band gap area, increasing their value for optoelectronics. Figure 11b depicts the optical transmittance spectra of all Na/Mg co-doped  $\text{TiO}_2$  compounds. These spectra were collected across a wavelength range of 300–700 nm. For wavelengths ranging from 420 to 700 nanometers, the transmittance spectra exhibit transparent behavior. These materials, on the other hand, can block light with wavelengths shorter than 420 nm because of the presence of the  $\text{TiO}_2$  absorption edge at 350 nm. The presence of this edge may explain this phenomenon. Furthermore, as demonstrated in the spectra, the transmittance value increases with Mg content, increasing from 81% to 84% for 8%Na/Mg co-doped  $\text{TiO}_2$ .

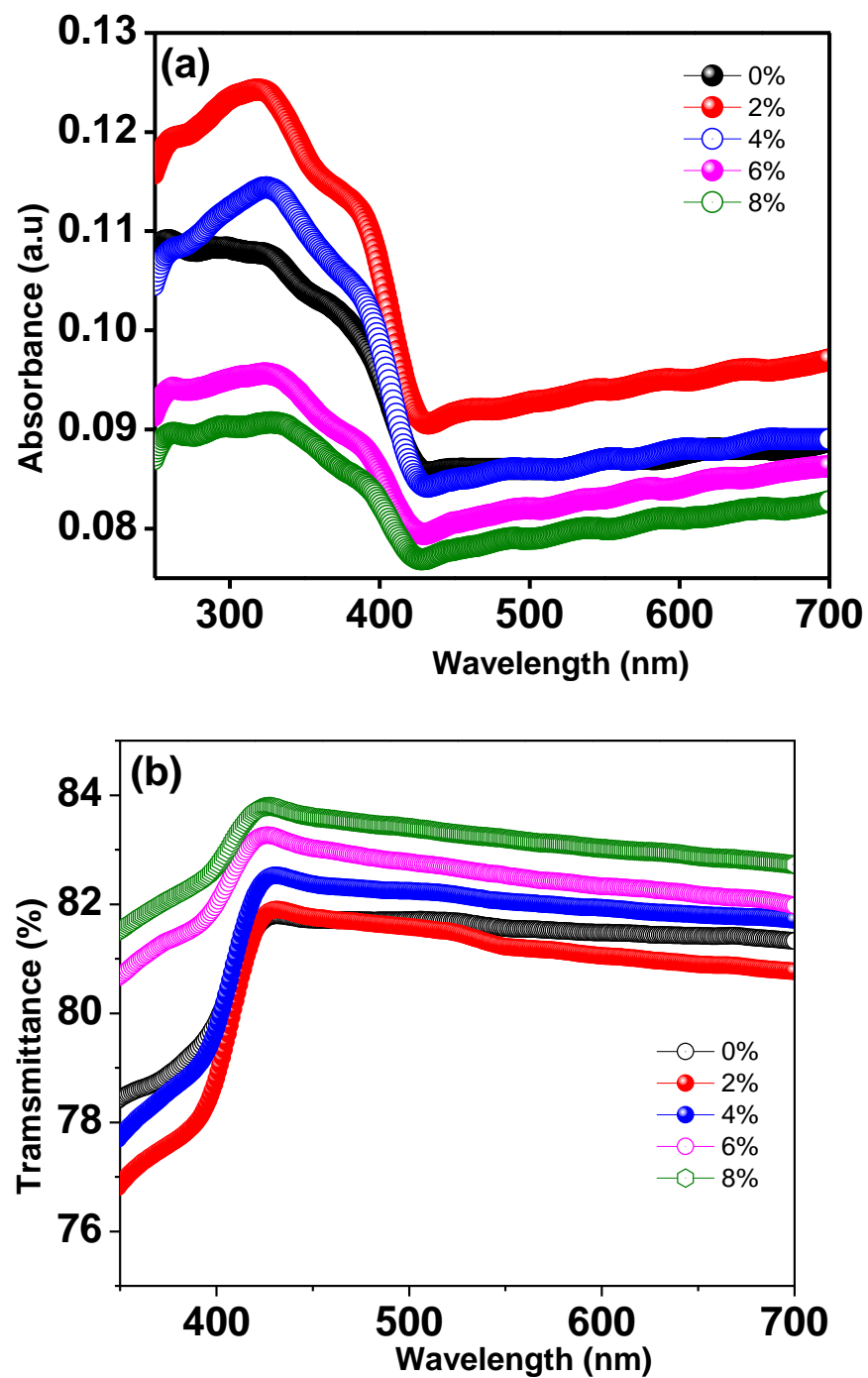


Figure 11. (a) UV-Visible absorption spectra of  $\text{Ti}_{0.94-y}\text{Na}_{0.06}\text{Mg}_y\text{O}_2$  with  $y = 0, 0.02, 0.04, 0.06, 0.08$  compounds and (b) UV-Visible transmittance spectra of  $\text{Ti}_{0.94-y}\text{Na}_{0.06}\text{Mg}_y\text{O}_2$  with  $y = 0, 0.02, 0.04, 0.06, 0.08$  compounds.

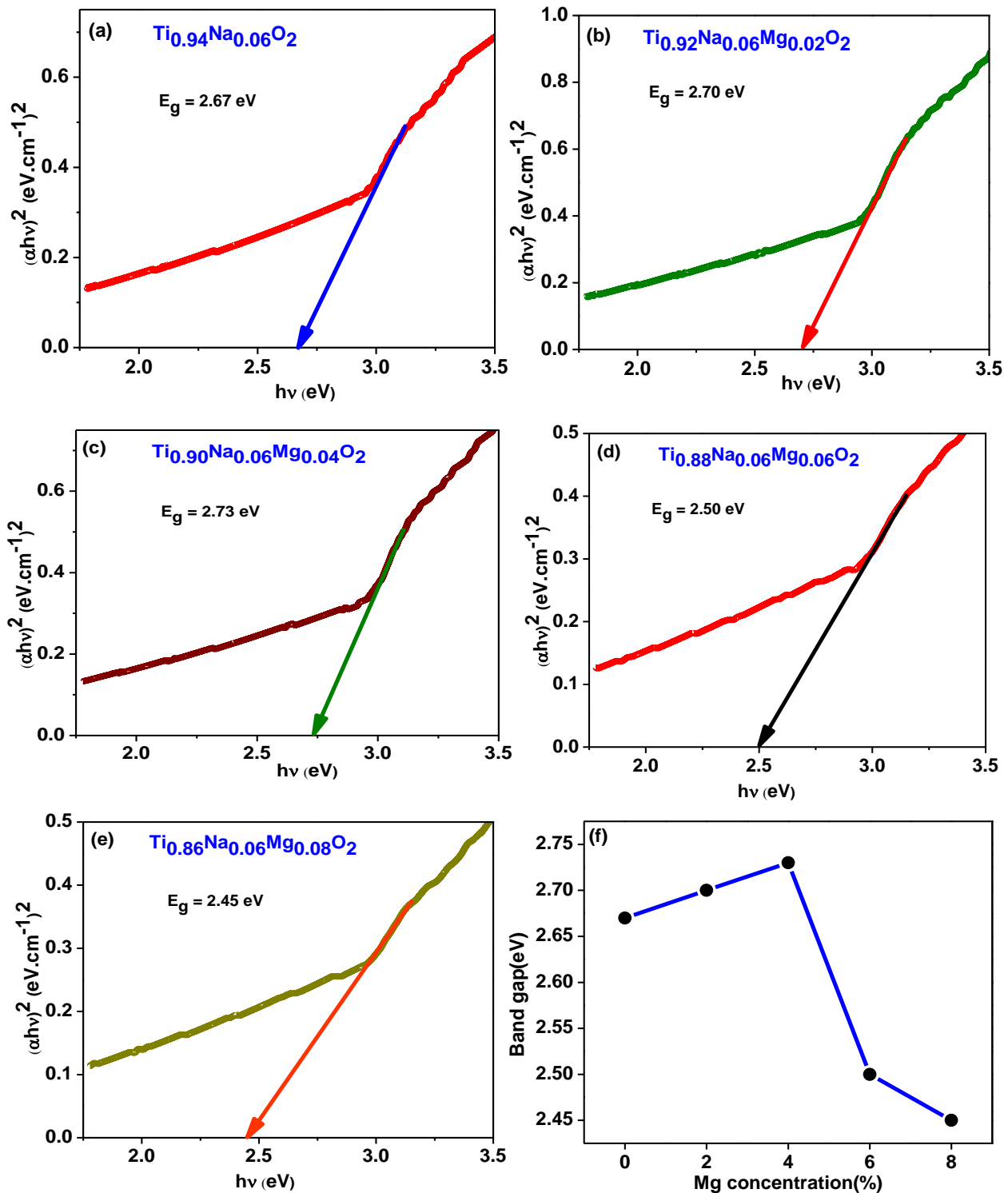
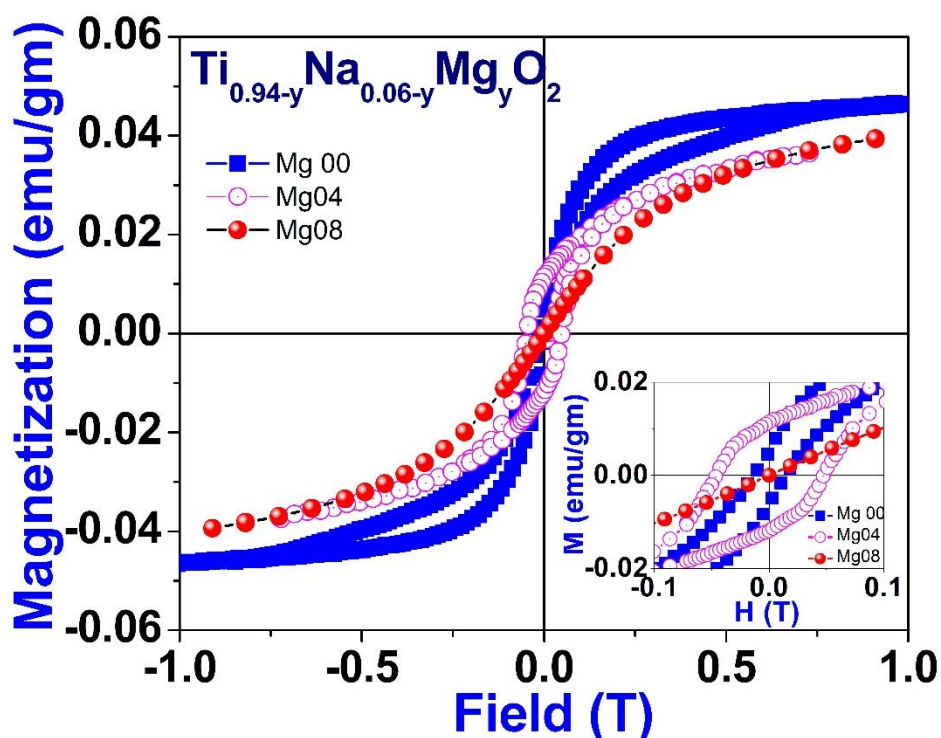


Figure 12. (a–e) depict the Tauc's plot generated from absorption spectra for Ti<sub>0.94-y</sub>Na<sub>0.06</sub>Mg<sub>y</sub>O<sub>2</sub> with  $y = 0, 0.02, 0.04, 0.06, 0.08$  compounds. Figure (f) illustrates the fluctuation of the band gap in TiO<sub>2</sub> with Na/Mg co-doping concentrations.

### 3.6. Magnetic Properties

Figure 13 illustrates the field variation of magnetization measurements, also known as M-H curves, which were acquired at room temperature for a particular composition of Na/Mg co-doped TiO<sub>2</sub> compounds, i.e., for Ti<sub>0.94-y</sub>Na<sub>0.06</sub>Mg<sub>y</sub>O<sub>2</sub> for  $y = 0, 0.04$  and  $0.08$  compound. These curves show that saturation of magnetism occurs in all co-doped

samples alongside coercivity, which is a characteristic indication of ferromagnetic behavior. This is indicated by the fact that the curves are concave. The partially enlarged view of the M-H loop within the low field area for these compounds is shown as an inset in Figure 13. The coercivity value comes out to be 470, 134, and 15 Oe, respectively. The levels of saturation magnetization, denoted by  $M_s$ , drop if there is an increase in the amount of magnesium present. The  $M_s$  value comes out to be 0.045, 0.039, and 0.038 emu/gm, respectively, for compounds with 0, 4, and 8% magnesium co-doping in  $\text{TiO}_2$ . Additionally, as the concentration of magnesium co-doping increases, the value of coercivity, or  $H_C$ , drops as well. The decrease in values of  $M_s$  and  $H_C$  implies that the ferromagnetic coupling is disrupted with increasing Mg co-doping concentration. This may be inferred from the fact that the values of  $M_s$  and  $H_C$  have decreased.



**Figure 13.** Room temperature field variation of magnetization for  $\text{Ti}_{0.94-y}\text{Na}_{0.06-y}\text{Mg}_y\text{O}_2$  with  $y = 0, 0.04, \text{ and } 0.08$  compounds.

#### 4. Conclusions

As a result, our investigations into the micro-structure, dielectric characteristics, optical properties, and magnetic properties of  $\text{Ti}_{0.94-y}\text{Na}_{0.06-y}\text{Mg}_y\text{O}_2$  with  $y = 0, 0.02, 0.04, 0.06, 0.08$  compounds synthesized using the conventional solid-state approach have resulted in a number of fascinating discoveries.

- Microstructure:

Micrographs taken using a scanning electron microscope (SEM) reveal that the particles are round and measure between 20 and 70  $\mu\text{m}$  in diameter. Elements were analyzed using energy dispersive x-ray to confirm that the synthesized compounds had similar elemental compositions to their precursors and that the elements were distributed uniformly throughout the complex.

- Oxidation states:

The XPS study suggests that Ti mostly resided in the  $\text{Ti}^{4+}$  oxidation state.

- Dielectric Properties:

The dielectric analysis shows that dielectric value and AC conductivity enhance with the increase of Na/Mg concentration. In addition to this, the compounds have a dielectric constant that is considerable and shows small dielectric loss. When analyzing a complicated impedance spectrum, grain and grain boundary conduction can be identified by configuring the Nyquist plot to correspond to an appropriate electrical circuit. It can be seen that when the concentration of co-doping increases,  $R_g$  and  $R_{gb}$  both go down, which is an indication that  $R$  is getting lower for the samples. Possible causes include surface roughness or lattice mismatch at the metal-semiconductor interface, as well as the impact of high  $R$  on carrier transport between the metal and the semiconductor.

- Nature of charge carrier and density:

Because the incorporation of Na and Mg into  $TiO_2$  results in the production of holes within the compounds, Hall effect tests reveal that all Na/Mg co-doped  $TiO_2$  compounds display p-type conductivity.

- Optical Properties:

The optical property measurement carried out using a UV-Vis spectrophotometer indicates without a shadow of a doubt that Na/Mg has been incorporated into the  $TiO_2$  matrix, which has led to a narrowing of the band gap. The transmittance value rises with increasing Mg concentration, going from 81% to 84% for 8%Na/Mg co-doped  $TiO_2$ .

- Magnetic Property:

It has been shown that room-temperature ferromagnetic behavior is displayed by all of the Na/Mg co-doped  $TiO_2$  compounds.

In conclusion, the use of Na/Mg co-doping on p-type  $TiO_2$  samples unlocks potential applications in spintronics, optoelectronics, magnetic media, and storage devices.

**Author Contributions:** R.N.: Investigation, Methodology, Formal analysis, Writing Manuscript; B.D.: Investigation; A.M., S.S. and B.N.P.: Investigation; S.R.: Visualization, Resources, Writing—Review and Editing, Supervision; S.K.S.: Conceptualization, Methodology, Visualization, Writing—Review and Editing, Supervision. All authors have read and agreed to the published version of the manuscript.

**Funding:** This research received no external funding.

**Institutional Review Board Statement:** Not Applicable.

**Informed Consent Statement:** Not Applicable.

**Data Availability Statement:** The data that supports the findings of this study are available within the article.

**Acknowledgments:** This present research work is not supported by any kind of research grant.

**Conflicts of Interest:** The authors declare no conflict of interest.

## References

1. Ohno, H. Making nonmagnetic semiconductors ferromagnetic. *Science* **1998**, *281*, 951–956. [[CrossRef](#)]
2. Chouhan, S.L.; Srivastava, K. A Comprehensive Review on Recent Advancements in d0 Ferromagnetic Oxide Materials for Spintronics Application. *Mater. Sci. Semicond. Process.* **2022**, *147*, 106768. [[CrossRef](#)]
3. Furdyna, J.K. Diluted magnetic semiconductors. *J. Appl. Phys.* **1988**, *64*, R29. [[CrossRef](#)]
4. Ogale, S.B.; Choudhary, R.J.; Buban, J.P.; Lofland, S.E.; Shinde, S.R.; Kale, S.N.; Kulkarni, V.N.; Higgins, J.; Lanci, C.; Simpson, J.R.; et al. High Temperature Ferromagnetism with a Giant Magnetic Moment in Transparent Co-doped  $SnO_{2-\delta}$ . *Phys. Rev. Lett.* **2003**, *91*, 077205. [[CrossRef](#)]
5. Wang, X.L.; Dai, Z.X.; Zeng, Z. Evidence of carrier mediated room temperature ferromagnetism in transparent semiconducting  $Sn_{1-x}Co_xO_{2-\delta}$  thin films. *J. Phys. Condens. Matter* **2008**, *20*, 125208.
6. Srivastava, S.K.; Lejay, P.; Barbara, B.; Boisson, O.; Pailhès, S.; Bouzerar, G. Absence of ferromagnetism in Mn-doped tetragonal zirconia. *J. Appl. Phys.* **2011**, *110*, 043929. [[CrossRef](#)]
7. Srivastava, S.K. Magnetic Property of Mn-Doped Monoclinic  $ZrO_2$  Compounds. *J. Supercond. Nov. Magn.* **2020**, *33*, 2501. [[CrossRef](#)]

8. Subramanian, M.; Thakur, P.; Tanemura, M.; Hihara, T.; Ganesan, V.; Soga, T.; Chae, K.H.; Jayavel, R.; Jimbo, T. Intrinsic ferro-magnetism and magnetic anisotropy in Gd-doped ZnO thin films synthesized by pulsed spray pyrolysis method. *J. Appl. Phys.* **2010**, *108*, 053904. [[CrossRef](#)]
9. Bryan, J.D.; Heald, S.M.; Chambers, S.A.; Gamelin, D.R. Strong Room-Temperature Ferromagnetism in Co<sup>2+</sup>-Doped TiO<sub>2</sub> Made from Colloidal Nanocrystals. *J. Am. Chem. Soc.* **2004**, *126*, 11640. [[CrossRef](#)]
10. Srivastava, S.K.; Brahma, R.; Datta, S.; Guha, S.; Baro, S.S.; Narzary, B.; Basumatary, D.R.; Kar, M.; Ravi, S. Effect of (Ni-Ag) co-doping on crystal structure and magnetic Property of SnO<sub>2</sub>. *Mater. Res. Express* **2019**, *6*, 126107. [[CrossRef](#)]
11. Srivastava, S.K.; Baro, S.S.; Narzary, B.; Basumatary, D.R.; Brahma, R.; Ravi, S. Crystal Structure and Magnetic Properties of (Co-Ag) co-doped SnO<sub>2</sub> Compounds. *J. Supercond. Nov. Magn.* **2021**, *34*, 461–467. [[CrossRef](#)]
12. Chouhan, L.; Bouzerar, G.; Srivastava, S.K. Effect of Mg-doping in tailoring d0 ferromagnetism of rutile TiO<sub>2</sub> compounds for spintronics application. *J. Mater. Sci. Mater. Electron.* **2021**, *32*, 11193. [[CrossRef](#)]
13. Osorio-Guillen, J.; Iany, S.; Barabash, S.V.; Zunger, A. Magnetism without Magnetic Ions: Percolation, Exchange, and Formation Energies of Magnetism-Promoting Intrinsic Defects in CaO. *Phys. Rev. Lett.* **2006**, *96*, 1072033. [[CrossRef](#)]
14. Pan, H.; Yi, J.B.; Shen, L.; Wu, R.Q.; Yang, J.H.; Lin, J.Y.; Feng, Y.P.; Ding, J.; Van, L.H.; Yin, J.H. Room-Temperature Ferromagnetism in Carbon-Doped ZnO. *Phys. Rev. Lett.* **2007**, *99*, 127201. [[CrossRef](#)]
15. Young, D.P.; Hall, D.; Torelli, M.E.; Fisk, Z.; Sarrao, J.L.; Thompson, J.D.; Ott, H.-R.; Oseroff, S.B.; Goodrich, R.G.; Zysler, R. High-temperature weak ferromagnetism in a low-density free-electron gas. *Nature* **1999**, *397*, 412–414. [[CrossRef](#)]
16. Máca, F.; Kudrnovský, J.; Drchal, V.; Bouzerar, G. Magnetism without magnetic impurities in ZrO<sub>2</sub> oxide. *Appl. Phys. Lett.* **2008**, *92*, 212503. [[CrossRef](#)]
17. Bouzerar, G.; Ziman, T. Model for Vacancy-Induced d0 Ferromagnetism in Oxide Compounds. *Phys. Rev. Lett.* **2006**, *96*, 207602. [[CrossRef](#)]
18. Narzary, R.; Dey, B.; Chouhan, L.; Kumar, S.; Ravi, S.; Srivastava, S. Optical band gap tuning, zero dielectric loss and room temperature ferromagnetism in (Ag/Mg) co-doped SnO<sub>2</sub> compounds for spintronics applications. *Mater. Sci. Semicond. Process.* **2022**, *142*, 106477. [[CrossRef](#)]
19. Srivastava, S.K.; Lejay, P.; Barbara, B.; Pailhès, S.; Madigou, V.; Bouzerar, G. Possible room-temperature ferromagnetism in K-doped SnO<sub>2</sub>: X-ray diffraction and high-resolution transmission electron microscopy study. *Phys. Rev. B* **2010**, *82*, 193203. [[CrossRef](#)]
20. Srivastava, S.K.; Lejay, P.; Hadj-Azzem, A.; Bouzerar, G. Non-magnetic Impurity Induced Magnetism in Li-Doped SnO<sub>2</sub> Nanoparticles. *J. Supercond. Nov. Magn.* **2014**, *27*, 487–492. [[CrossRef](#)]
21. Wang, J.; Zhou, D.; Li, Y.; Wu, P. Experimental and first-principle studies of ferromagnetism in Na-doped SnO<sub>2</sub> nanoparticles. *Vacuum* **2017**, *141*, 62–67. [[CrossRef](#)]
22. Chouhan, L.; Panda, S.K.; Bhattacharjee, S.; Das, B.; Mondal, A.; Parida, B.; Brahma, R.; Manglam, M.K.; Kar, M.; Bouzerar, G.; et al. Room temperature d0 ferromagnetism, zero dielectric loss and ac-conductivity enhancement in p-type Ag-doped SnO<sub>2</sub> compounds. *J. Alloy. Compd.* **2021**, *870*, 159515. [[CrossRef](#)]
23. Srivastava, S.K.; Lejay, P.; Barbara, B.; Boisson, O.; Pailhès, S.; Bouzerar, G. Non-magnetic impurity induced magnetism in rutile TiO<sub>2</sub>:K compounds. *J. Phys. Condens. Matter* **2011**, *23*, 442202. [[CrossRef](#)]
24. Chouhan, L.; Srivastava, S. Observation of room temperature d0 ferromagnetism, band-gap widening, zero dielectric loss and conductivity enhancement in Mg doped TiO<sub>2</sub> (rutile + anatase) compounds for spintronics applications. *J. Solid State Chem.* **2022**, *307*, 122828. [[CrossRef](#)]
25. Chouhan, L.; Narzary, R.; Dey, B.; Panda, S.K.; Manglam, M.K.; Roy, L.; Brahma, R.; Mondal, A.; Kar, M.; Ravi, S.; et al. Tailoring room temperature d0 ferromagnetism, dielectric, optical, and transport properties in Ag-doped rutile TiO<sub>2</sub> compounds for spintronics applications. *J. Mater. Sci. Mater. Electron.* **2021**, *32*, 28163–28175. [[CrossRef](#)]
26. Hou, D.L.; Meng, H.J.; Jia, L.Y.; Ye, X.J.; Zhou, H.J.; Li, X.L. Impurity concentration study on ferromagnetism in Cu-doped TiO<sub>2</sub> thin films. *Eur. Lett.* **2007**, *78*, 67001. [[CrossRef](#)]
27. Duhalde, S.; Vignolo, M.F.; Golmar, F.; Chilotte, C.; Torres, C.E.R.; Errico, L.A.; Cabrera, A.F.; Rentería, M.; Sánchez, F.H.; Weissmann, M. Appearance of room-temperature ferromagnetism in Cu-doped TiO<sub>2</sub>- $\delta$  films. *Phys. Rev. B* **2005**, *72*, 161313. [[CrossRef](#)]
28. Dimri, M.C.; Khanduri, H.; Kooskora, H.; Kodu, M.; Jaaniso, R.; Heinmaa, I.; Mere, A.; Krustok, J.; Stern, R. Room-temperature ferromagnetism in Ca and Mg stabilized cubic zirconia bulk samples and thin films prepared by pulsed laser deposition. *J. Phys. D Appl. Phys.* **2012**, *45*, 475003. [[CrossRef](#)]
29. Chouhan, L.; Bouzerar, G.; Srivastava, S. d0 Ferromagnetism in Ag-doped monoclinic ZrO<sub>2</sub> compounds. *Vacuum* **2020**, *182*, 109716. [[CrossRef](#)]
30. Chawla, S.; Jayanthi, K.; Kotnala, R.K. High temperature carrier controlled ferromagnetism in alkali doped ZnO nanorods. *J. Appl. Phys.* **2009**, *106*, 113923. [[CrossRef](#)]
31. Chouhan, L.; Bouzerar, G.; Srivastava, S.K. d0 ferromagnetism in Li-doped ZnO compounds. *J. Mater. Sci. Mater. Electron.* **2021**, *32*, 6389–6397. [[CrossRef](#)]
32. Sharma, N.; Kant, R.; Sharma, V.; Kumar, S. Influence of Silver Dopant on Morphological, Dielectric and Magnetic Properties of ZnO Nanoparticles. *J. Electron. Mater.* **2018**, *47*, 4098–4107. [[CrossRef](#)]

33. Deng, R.; Yao, B.; Li, Y.F.; Xu, Y.; Li, J.C.; Li, B.H.; Shen, D.Z. Ultraviolet electroluminescence from n-ZnO/p-NiO heterojunction light-emitting diode. *J. Lumin.* **2013**, *134*, 240. [[CrossRef](#)]
34. Ahmed, F.; Kumar, S.; Arshi, N.; Anwar, M.S.; Heo, S.N.; Kim, G.W.; Lu, J.; Koo, B.H. Room-temperature Ferromagnetism in Cu-doped ZnONanorods Prepared Using a Microwave Irradiation Method. *J. Korean Phys. Soc.* **2012**, *60*, 1644. [[CrossRef](#)]
35. Li, J.; Li, Y.; Li, S.; Zhu, M.; Zhang, J.; Li, Y.; He, Y.; Li, W. Zinc interstitial and oxygen vacancy mediated high Curie-temperature ferromagnetism in Ag-doped ZnO. *Ceram. Int.* **2020**, *46*, 18639–18647. [[CrossRef](#)]
36. Dey, B.; Narzary, R.; Chouhan, L.; Bhattacharjee, S.; Parida, B.N.; Mondal, A.; Ravi, S.; Srivastava, S.K. Crystal structure, optical and dielectric properties of Ag:ZnO composite-like compounds. *J. Mater. Sci. Mater. Electron.* **2022**, *33*, 2855. [[CrossRef](#)]
37. Chakraborti, D.; Narayan, J. Room temperature ferromagnetism in Zn<sub>1-x</sub>Cu<sub>x</sub>O thin films. *Appl. Phys. Lett.* **2007**, *90*, 062504. [[CrossRef](#)]
38. Chawla, S.; Jayanthi, K.; Kotnala, R.K. Room-temperature ferromagnetism in Li-doped p-type luminescent ZnONanorods. *Phys. Rev. B* **2009**, *79*, 125204. [[CrossRef](#)]
39. Dey, B.; Srivastava, S.K. Crystal structure, microstructure, optical, dielectric and magnetic properties of TiO<sub>2</sub> nanoparticles. *J. Mater. Sci. Mater. Electron.* **2022**, *33*, 23506–23514. [[CrossRef](#)]
40. Ghosh, S.; Khan, G.G.; Das, V.; Mandal, K. Vacancy-induced intrinsic d0 ferromagnetism and photoluminescence in potassium doped ZnO nanowires. *J. Appl. Phys.* **2011**, *109*, 123927. [[CrossRef](#)]
41. Huang, Y.; Zhou, W.; Wu, P. Room-temperature ferromagnetism in epitaxial p-type K-doped ZnOfilms. *Solid State Commun.* **2014**, *183*, 31. [[CrossRef](#)]
42. Dey, B.; Narzary, R.; Panda, S.K.; Mallick, J.; Mondal, A.; Ravi, S.; Kar, M.; Srivastava, S. Room temperature d0 ferromagnetism, band-gap reduction, and high optical transparency in p-type K-doped ZnO compounds for spintronics applications. *Mater. Sci. Semicond. Process.* **2022**, *148*, 106798. [[CrossRef](#)]
43. Zhang, H.; Wang, Y.; Wang, H.; Huo, D.; Tan, W. Room-temperature magnetoresistive and magnetocaloric effect in La<sub>1-x</sub>Ba<sub>x</sub>MnO<sub>3</sub> compounds: Role of Griffiths phase with ferromagnetic metal cluster above Curie temperature. *J. Appl. Phys.* **2022**, *131*, 043901. [[CrossRef](#)]
44. Dey, B.; Panda, S.K.; Mallick, J.; Sen, S.; Parida, B.; Mondal, A.; Kar, M.; Srivastava, S. Observation of room temperature d0 ferromagnetism, bandgap narrowing, zero dielectric loss, dielectric enhancement in highly transparent p-type Na-doped rutile TiO<sub>2</sub> compounds for spintronics applications. *J. Alloy. Compd.* **2023**, *930*, 167442. [[CrossRef](#)]
45. Koops, C.G. On the Dispersion of Resistivity and Dielectric Constant of Some Semiconductors at Audiofrequencies. *Phys. Rev. (Series I)* **1951**, *83*, 121–124. [[CrossRef](#)]
46. Srivastava, S.K.; Ravi, S. The Effect of Co Substitution on the Crystal Structure and Electrical Resistivity of (La<sub>0.85</sub>Ag<sub>0.15</sub>)MnO<sub>3</sub> Compounds. *J. Supercond. Nov. Magn.* **2009**, *22*, 651–658. [[CrossRef](#)]
47. Srivastava, S.K.; Kar, M.; Ravi, S. Ferromagnetic insulating and spin glass behavior in Cr substituted La<sub>0.85</sub>Ag<sub>0.15</sub>MnO<sub>3</sub> compounds. *J. Phys. Condens. Matter* **2008**, *20*, 235201. [[CrossRef](#)]
48. Tauc, J.; Grigorovici, R.; Vancu, A. Optical Properties and Electronic Structure of Amorphous Germanium. *Phys. Status Solidi B* **1966**, *15*, 627–637. [[CrossRef](#)]